THE JOURNAL OF PHYSICAL CHEMISTRY C

Article

pubs.acs.org/JPCC

Spectroscopic *in situ* Measurements of the Relative Pt Skin Thicknesses and Porosities of Dealloyed PtM_n (Ni, Co) Electrocatalysts

Keegan M. Caldwell and David E. Ramaker*

Department of Chemistry, George Washington University, Washington, District of Columbia 20052, United States

Qingying Jia and Sanjeev Mukerjee

Department of Chemistry and Chemical Biology, Northeastern University, Boston, Massachusetts 02115, United States

Joseph M. Ziegelbauer, Ratandeep S. Kukreja, and Anusorn Kongkanand

Electrochemical Energy Research Laboratory, General Motors Central Research and Development, Warren, Michigan 48090, United States

ABSTRACT: X-ray adsorption near edge structure (XANES) data at the Co or Ni K-edge, analyzed using the $\Delta\mu$ difference procedure, are reported for dealloyed $PtCo_x$ and $PtNi_x$ catalysts (six different catalysts at different stages of life). All catalysts meet the 2017 DOE beginning of life target Pt mass activity target (>0.44 A mg_{Pt}^{-1}), but exhibit varying activities and durabilities. The variance factors include different initial precursors, dealloying in HNO_3 vs H_2SO_4, if a postdealloying thermal annealing step was performed, and different morphologies (some with a multi PtM_x core and porous Pt skin, some single core with nonporous skin). Data are obtained at the initial beginning of life (BOL, ~200 voltage cycles) and after 10k and 30k (end of life, EOL) voltage cycles following DOE protocol (0.6−1.0 V vs reversible hydrogen electrode). The $\Delta\mu$ data are used to determine at what potential (V_{pen}) the Pt skin is penetrated by O. The durability, related to a drop in the electrochemical surface areas (ECSAs) after extensive voltage cycling, directly correlates with the V_{pen} at BOL. The data indicate that cycling produces a "characteristic" Pt skin robustness (porosity or thickness). When the Pt skin at BOL is "thin" (V_{pen} < 0.9 V) it grows to a "characteristic" thickness consistent with a V_{pen} of ≈1.1 V, and if it begins very thick, it thins to the same "characteristic" thickness. Particles dealloyed in H_2SO_4 appear to have a thicker Pt skin at BOL than those dealloyed in HNO_3, and a postdealloying annealing procedure appears to produce a particularly nonporous skin with high V_{pen}, but not necessarily thicker. Furthermore, the PtM_3 catalysts exhibited a fast skin "healing" process whereby the initial porous skin appears to become more nonporous after holding the potential at 0.9 V. This work is believed to be the first *in situ* XAS study to shed light on the nature of the Pt skin, its thickness, and/or porosity, and how it changes with respect to operating electrochemical conditions.

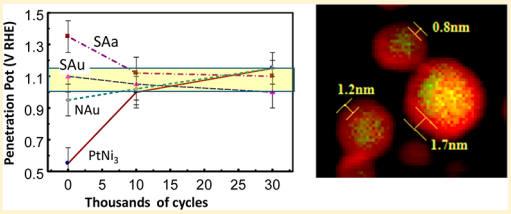

INTRODUCTION

Our continued reliance on fossil fuels and the internal combustion engine to meet the increasing global demand for personal transportation will cause a continued increase in greenhouse gas emissions and likely drive global temperature rise. To eliminate the contribution of personal transportation to CO_2 emissions, we need technologies that will enable a shift to "zero-emission" transportation; and commercially viable proton-exchange membrane fuel cells (PEMFCs) would provide such an option. The higher energy conversion efficiencies of fuel cells make them a high value target even with today's fossil fuels, particularly residential and commercial applications,[1−4] and ultimately PEMFCs could dramatically reduce carbon emissions with H_2 the energy carrier. Major hurdles in the commercialization of PEMFC's are the high cost of Pt and the kinetically sluggish oxygen reduction reaction (ORR) rate.[5−7] Enhancing the catalytic activity while maintaining durability and driving down the costly Pt content required in PEMFC's has remained a challenge for several years.[8,9] The United States Department of Energy (DOE) has promulgated a 2017 target Pt mass activity of 0.44 A mg_{Pt}^{-1} at 0.9 V for the ORR mass activity with less than a 40% loss after 30 000 cycles.[10]

Many studies have been conducted on bimetallic or multimetallic nanoparticles.[11−18] Recent density functional theory (DFT) studies on Pt_3Co and Pt_3Ni catalysts show

Received: September 29, 2014
Revised: December 5, 2014
Published: December 5, 2014

that both the activity and stability are related to the overall alloy composition and the surface atomic distribution.[19] Studies conducted by Strasser et al.[13,20] have shown that dealloyed $PtNi_3$ catalysts show an ORR mass activity 7−8 times greater than the pure Pt mass activity (with similar enhancements in the Pt surface specific activity) along with long-term stability. These dealloyed materials are shown to have mostly core−shell structures with Pt-rich shells and $PtNi_x$ cores. The surface morphologies and electronic structures of similar core−shell catalysts have been studied using density functional theory (DFT), and these theoretical results reveal that the enhancement can be attributed to the reduced Pt−Pt distance in the outer shell (the so-called geometric effect).[13−20] The lattice reduction of the Pt "skin" occurs because of the smaller lattice spacing in the $PtNi_3$ core. This geometric effect apparently occurs in addition to the more common ligand or electronic effect that results from M atoms existing near the particle surface. In fact the exact role that each of these plays in enhancing the ORR activity in the dealloyed PtM particles is still controversial.[21]

The dealloyed particles are prepared by either acid leaching or electrochemically removing nearly 90% of the more reactive M element from the initial PtM_3 precursors, resulting in a material that is $Pt_{1.5-5}M$, with the outer atomic layers almost totally without M. It is a challenge with either process to create dealloyed nanocatalyst particles that possess a uniform core−shell morphological structure, due to lack of synthetic control over the dealloying process.[22−29] Often the final Pt_nM particles are found to have multicores, sometimes with M atoms still at or on the surface, sometimes not, and yet many of these different morphologies appear to have similar enhanced ORR activities.[13] Clearly the roles of the ligand vs the geometric effects are both important, and the interplay between these two mechanisms is not clear. It appears that the well-formed single core−shell particles with a Pt outer shell of several monolayers are the most durable,[30] but no systematic way has yet been found to prepare exclusively the preferred particles. Furthermore, the catalytic ORR activity has not even shown a systematic correlation with particle structure. Clearly more work is required in this area.

The rational design of electrocatalysts for commercial fuel cell applications requires an understanding of the Pt catalyzed electrochemical reduction of oxygen to water, $O_2 + 4H^+ + 4e^- \rightarrow 2H_2O$. The mechanism of this reaction involves many steps and there is some debate about the exact pathway this reaction takes. Markovic et al. proposed[14] that the area specific kinetic current density i at potential E is a function of the Gibbs free energy of adsorption, ΔG_{ads}, of the hydroxyl intermediate on a Pt atom. This concept has generally been accepted by the scientific community, and if true, it means that manipulation of the physical structure, and hence the electronic structure of the outer Pt surface, can delay the onset of OH adsorption, which blocks Pt sites for O_2 adsorption and thereby decreases the specific ORR. However, other new studies suggest that it is not only the hydroxyl adsorption which maintains mechanistic control, but the adsorption of other intermediate species.[31,32]

X-ray adsorption spectroscopy (XAS) is an element specific, core level spectroscopic technique that can be used *in operando* under a wide range of electrochemical and fuel cell (full or half cell) operating conditions because a light beam simply needs to be able to pass through the system in this technique.[33−37] It is ideal for providing information on small particles because the extended X-ray absorption fine structure (EXAFS) arises from the short-range photoelectron scattering (i.e., these electrons lose energy after just a few scattering steps), as opposed to X-ray diffraction (XRD) that reflects the much longer range photon scattering. XAS, like many other spectroscopic techniques, sums and averages over all atoms equally thus hindering its ability to elucidate surface chemistry. The $\Delta\mu$-XANES analysis,[38,39] which takes the difference $\Delta\mu = \mu(\text{Ad/Pt}) - \mu(\text{Pt})$, overcomes this limitation by subtracting out any part of the spectrum that did not change (i.e., the bulk interior) and highlighting the part that did change at the surface, thereby providing a surface sensitive technique capable of reflecting the relative coverage of specific adsorbates (Ad) on the surface, such as OH, O, H, and CO, and their binding sites (e.g., 3-fold, atop, etc.).

XAS and $\Delta\mu$-XANES studies have been reported on a variety of PtM fuel cell catalyts.[30,31,33−36] These studies were conducted in conjunction with theoretical DFT calculations of the adsorption energies[40] of ORR intermediates (e.g., OH_{ads}, O_2, and OOH_{ads}) to allow for the estimation of the surface coverages of these species under fuel cell operating conditions. In general, these calculations suggest a volcano like reactivity curve versus the binding energy of some intermediate in the reaction. This is typical of nearly all catalytic reactions. This volcano-like curve appears because the reactant must bind to the surface, react, and then the product must leave. If the binding is too weak, the reaction is too slow, if it is too strong, the product cannot get off of the catalyst surface and thus poisons sites for other reactants. In the ORR this volcano curve follows the Sabatier model[41] with the Pt−O bond strength being the critical variable. If the Pt−O binding is too weak, dioxygen molecular species such as O_2 or OOH build up and poison the surface, if too strong mono-oxygen species such as OH and H_2O poison the surface.

Although theoretical and electrochemical studies have indicated the buildup of OH when the Pt−O binding is too strong,[13,42] very few if any spectroscopic techniques have observed a buildup of dioxygen-type species when the O binding becomes too weak; although as noted above theoretical DFT calculations indicate this. The dramatic changes occurring in the size, morphology, and oxidation state of Pt−M catalysts under the harsh operating conditions of fuel cells makes it almost useless to compare *in situ* with *ex situ* results. Therefore, realistic studies must be performed *in situ* so that one can distinguish between the kinetic contributions of different electrocatalysts to the ORR activity and the particle morphology. Unfortunately very few if any spectroscopic techniques are able to follow the coverage of molecular adsorbates in the presence of H_2O electrolyte on a real supported Pt catalyst surface. We have recently shown that this is possible with the $\Delta\mu$ XANES technique.[43]

Understanding the durability and its dependence on particle morphology requires knowledge of many properties such as the final Pt/Ni atomic ratios, outer Pt skin thickness, and the nature of the Pt sites on the outer surface, which are properties difficult to experimentally obtain. In this work we obtained information on the relative Pt skin thicknesses and/or porosity. We then used high angle annular dark field (HAADF) STEM with electron energy loss spectroscopy (EELS) to measure the Pt skin thicknesses in order to validate our study. To the best of our knowledge, this is the first *in situ* XAS study to shed light on the nature of the Pt skin, its thickness, and porosity and thereby shed light on how it related to the ORR in a fuel cell.

dx.doi.org/10.1021/jp5098553 | J. Phys. Chem. C 2015, 119, 757−765

Table 1. Summary of Studied Electrocatalysts

catalyst symbol	precursor[a]	acid used for dealloying	t/T	post annealing[b]	life stages measured[c]	morphology[d]
$PtNi_3$	$PtNi_3$	HNO_3	24/80	no	BOL, 10k, 30k	mc−ps
PtCo	PtCo	HNO_3	24/80	no	BOL	sc−ns
$PtCo_3$	$PtCo_3$	HNO_3	24/80	no	BOL	50% mc−ps,50% sc-ns
NAu	$PtNi_3$	HNO_3	24/70	no	BOL, 10k, 30k	sc−ns
SAu	$PtNi_3$	H_2SO_4	24/80	no	BOL, 10k, 30k	sc−ns
SAa	$PtNi_3$	H_2SO_4	24/80	yes	BOL, 30k	sc−ns

[a]PtM indicates atomic ratio of metals in precursor before dealloying. Note that the catalyst labeled "PtM_3" were prepared from a different type precursor than the catalysts NAu, SAu, and SAa. [b]Post annealed with a thermal treatment in 5% H_2/N_2 at 400 °C for 4 h. [c]BOL (beginning of life, following 1 day of fuel cell operation), 10k (post 10k voltage cycles), 30k (post 30k voltage cycles). [d]Morphology description obtained from HAADF data: either multi- or single core PtM_x (mc or sc) with porous or nonporous Pt skin (ps or ns).

EXPERIMENTAL SECTION

Electrochemical Dealloying, MEA Preparation, and ORR Testing. We recently reported XANES data at the Pt L_3 edge on dealloyed $PtCo_x$ and $PtNi_x$ catalysts (six different catalysts at three different stages of life) as summarized in Table 1.[40] Further we reported Co edge data on the PtCo catalysts previously.[44] Here we report XANES results at the Ni or Co K edge for the remaining catalysts in Table 1. The factors include, as summarized in Table 1, the $PtCo_x$ or $PtNi_3$ precursor, the acid used for leaching the Ni or Co (HNO_3 or H_2SO_4 denoted NA or SA), the dealloying time in hours and temperature in °C (t/T), and the use of a postdealloying thermal anneal in 5% H_2/N_2 at 400 °C for 4 h (denoted *un-a*nnealed or *a*nnealed). The details of the MEA preparation are described in the literature.[40,41] Initial (BOL) ORR mass activities (A mg_{Pt}^{-1} at 0.9 V vs RHE) and that after 10k and 30k cycles (following DOE protocol[12]) have been measured and reported elsewhere.[27] All catalysts meet the DOE 2017 BOL Pt mass activity target (0.44 A mg_{Pt}^{-1} at 0.9 $V_{iR\ free}$ and loss of <40% after 30k cycles[12]) but exhibit widely varying durabilities.

***In Situ* XAS Collection/Analysis.** The XAS experiments were collected using a flow-through cell configured following the procedure reported by Arruda et al.[45] and allows the user to oxygenate/deoxygenate the electrolyte during data collection at the beamline. XAS data can be collected in both fluorescence and transmission mode, and the cell was constructed from Teflon. The cell was flooded with deoxygenated 0.1 M $HClO_4$ electrolyte (performed with N_2 (or Ar) sparging) as well as after O_2 sparging, during operation. In addition to *in situ* data collection on fresh samples (beginning of life, BOL), experiments were performed on samples after aging using 10k and 30k cycling (0.6−1.0 V using DOE protocol[12]) to identify the degradation modes. Full range Co and Ni K edge EXAFS data were collected at various potentials along the anodic sweep of cyclic voltammograms (CVs). All XAS signals were collected with a beam spot size of 1 × 5 mm in the fluorescence mode with a 31-element fluorescence detector at the X3-B beamline (National Synchrotron Light Source, Brookhaven National Laboratory, Upton, NY). Transmission data were also collected with a thin Co or Ni foil for Co and Ni samples respectively to account for the shifts in energy due to variances in the monochromator position. The XAS alignment, background subtraction, and normalization of the XAS data were completed using the IFEFFIT suite.[46,47]

The $\Delta\mu$ signals are generated using the subtractive method, $\Delta\mu = \mu_{ads} - \mu_{clean}$, thereby removing the absorption from the bulk of the M in the $Pt_nM(Co,Ni)$ clusters. This relationship can be described as follows:

$$\Delta\mu(V) = \mu(\text{ad/M, V in } N_2 \text{ or } O_2,) - \mu(\text{M, 0.54 V in } N_2,) \quad (1)$$

where 0.54 V in N_2 is taken as the conditions when the Pt electrode is the cleanest or free of "ordered" adsorbates. Of course anions and water may be physisorbed on the Pt surface under these conditions, but previous studies have shown that these produce a small or negligible contribution to the XANES scattering, because of disorder and nonregistry with the Pt atoms on the surface.[35,36] Theoretical XANES spectra are obtained using the FEFF 8.0 code[48] which performs full multiple scattering calculations on a model cluster[49] (typically Pt_4M_2) representing the catalysts. These theoretical XANES spectra are used to obtain theoretical $\Delta\mu = \mu(ad/Pt_4M_2) - \mu(Pt_4M_2)$, signatures that can then be compared with the experimental data to identify unique adsorbate signatures.[34−36,40]

Microscopy. All TEM in the work was performed on JEOL 2100F S/TEM equipped with high resolution polepiece (HRP) and a probe spherical aberration (Cs) corrector, giving a point resolution of 0.14 nm. High angle annular dark field (HAADF) scanning TEM (STEM) images were formed by aligning the Ronchigram with the optic axis and a 40 μm condenser aperture with the center of the Ronchigram. A camera length of 10 cm was used to minimize the effect of diffraction contrast on the HAADF images. Electron energy loss spectroscopy (EELS) analysis was performed using a postcolumn GIF Tridiem system from Gatan Inc.

RESULTS

$\Delta\mu$ Analysis. Figure 1 shows theoretical $\Delta\mu$ signatures from FEFF 8.0 calculations for two different adsorbate sites on a cluster model as previously reported.[41] Our interpretation of the experimental Co k-edge $\Delta\mu$ line shapes is made possible by comparing these experimental results with the theoretical signatures. Here, the theoretical signatures show O atoms bonded in two different sites; namely, all to a neighboring Pt atom on the left or some directly to a Co atom on the right. In the first bonding arrangement, the influence on the Co must arise primarily from an electronic or ligand effect as the direct scattering from the O atom to the Co atom will be minimal. In the second site, O atoms are in direct "contact" or bonding with the Co as schematically shown. The $\Delta\mu$ calculation uses either the direct or ligand interaction for a much smaller Ad/Pt_4Co_2 cluster and subtracts that calculated for a similar clean Pt_4Co_2 cluster (no O adsorbate) to isolate the effects of the O adsorbate, as reported many time previously.[34−36,40]

We can compress the data for the different catalysts and follow more closely the changeover from the ligand to the

dx.doi.org/10.1021/jp5098553 | J. Phys. Chem. C 2015, 119, 757−765

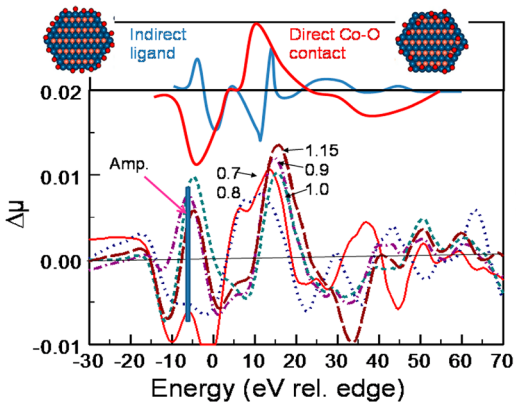

Figure 1. Co K edge $\Delta\mu$ for dealloyed $PtCo_3$ in N_2 shown at the indicated potentials. Directly above the experimental results are FEFF 8.0 calculated lineshapes for both the direct and the ligand effect signatures as given previously.[41] Schematic clusters are also shown illustrating the indirect electronic interaction between the O (red) and Co atoms (pink) and the direct contact after penetration of the outer Pt (blue atoms) skin.

direct signature by plotting the magnitude of the feature around −5 eV with potential. This feature is highlighted by the vertical bar in Figure 1. When this feature is positive, it indicates the ligand $\Delta\mu$ signature and when negative the direct signature. Thus, the point when the $\Delta\mu$ magnitude, $|\Delta\mu|$, crosses zero we call the "penetration" potential. The $|\Delta\mu|$ are plotted in Figure 2

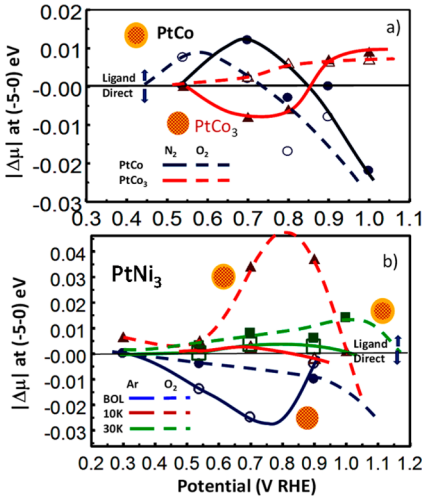

Figure 2. Co K edge $\Delta\mu$-XANES magnitude $|\Delta\mu|$ vs potential for dealloyed PtCo and $PtCo_3$ at BOL and Ni K-edge $PtNi_3$ at the 3 stages of life in N_2 or O_2-sparged 0.1 M $HClO_4$ as indicated. Schematic thick and thin outer Pt skins are shown for the different catalysts as discussed.

after N_2 sparging and after O_2. In N_2, the O(H) arises only from water activation, which begins on 3 nm clusters around 0.6 V, and we see the $|\Delta\mu|$ increasing at this point with the penetration potential for PtCo falling around 0.85 V. Note that on this plot $|\Delta\mu|$ in N_2 at 0.54 V is by definition zero, as dictated by eq 1. The effect of O_2 is to allow earlier adsorption of oxygen species on the surface, from oxygen reduction, therefore $|\Delta\mu|$ increases earlier, and the penetration potential is normally about 0.1 V earlier than for N_2.

The visual schematics in Figure 1 suggest why with increasing voltage the $\Delta\mu$ signature changes from the ligand to direct signature. The subsurface Co does not initially bind O at low potentials but as the potential increases, the oxygen is able to penetrate the outer Pt shell of the nanoparticle and bind directly to the Co. It is well-known that O can undergo place exchange with Pt and penetrate the surface at potentials near and above 0.9 V.[36] The single core (sc) nonporous (np) shell structure of the PtCo nanoparticles suggested by the Co K edge $\Delta\mu$-XANES analysis here has been further confirmed by *ex situ* HAADF/electron energy loss spectroscopy (EELS) data, which show that nearly all particles reveal a single core with a well-formed Pt outer shell.[50]

In contrast, the structural morphology of the dealloyed $PtCo_3$ catalysts, as revealed by HAADF/EELS, shows a "multicore" (mc) structure, with several $PtCo_x$ cores, particularly in the larger particles, and a porous Pt outer shell (ps). Statistical analysis of many PtCo particles revealed by HAADF data indicates that about 50% are mc-ps with about 50% sc-ns.[46,51] The Co $\Delta\mu$- XANES signatures for the dealloyed $PtCo_3$ catalyst in Figure 1 show large negative features in the −10 to 0 eV region already at low potentials; i.e., better agreement with the direct signature. These XAS results complement the HAADF/EELS results confirming the porous Pt skin, and further support our analysis that identifies O penetration and immediate direct Co−O binding.

As noted in Figure 2a, the behavior of $|\Delta\mu|$ is quite different for $PtCo_3$ with its mc-ps structure. In N_2, $|\Delta\mu|$ begins negative, i.e. indicating the direct contact signature as expected, but then a very interesting occurrence occurs; $|\Delta\mu|$ goes positive. Further in O_2, $|\Delta\mu|$ data taken on the same $PtCo_3$ sample after the run in N_2, begins positive and stays positive. This would suggest that the porous Pt skin existing initially became nonporous or "healed" in some way. We will discuss this in light of other results more fully below.

Similar $|\Delta\mu|$ results for a dealloyed $PtNi_3$ catalyst, but now using the Ni K edge $\Delta\mu$ XANES data, is shown in Figure 2b. The $\Delta\mu$ signatures, not shown here, are similar to those found for Co with the two $PtCo_x$ samples above. Further, we now show data for $PtNi_3$ with aging, i.e. at the beginning of life (BOL with just 200 cycles for break-in), and then after 10k and 30k cycles (EOL) using DOE protocol as described above. The data clearly reveal the growing robustness (thickness or nonporosity) of the Pt skin with cycling on these dealloyed PtNi catalysts, as the penetration potential increases with cycling. HAADF/EELS data show that the $PtNi_3$ catalyst at BOL has a multicore structure with a porous Pt skin (ms-ps).[52] The initial negative $|\Delta\mu|$ for the BOL samples confirms that the O is able to gain access to the Ni already at low potentials due to the porous skin. After cycling for 10k, the Pt skin is significantly enhanced, since penetration by the O is not evident until around 0.85 V. Finally after 30k cycles, the penetration potential in N_2(Ar) appears to be above the measured potential range; near 1.1 V, but unfortunately the lack of further points makes this less clear. Note that again in N_2(Ar), the $PtNi_3$ BOL catalyst appears to show a healing similar to that in $PtCo_3$.

The difference between the data in N_2 vs O_2 in Figure 2b is quite revealing of the competition for Pt adsorption sites. For the BOL sample, $|\Delta\mu|$ is less negative in O_2, but for the 10k and 30k cycles, it is more positive; i.e., it is always shifted up in O_2 relative to N_2 because the amount of surface adsorbate coverage is higher. The larger ligand effect in O_2 compared to N_2 (10k and 30k samples) clearly arises from the additional adsorbed dioxygen type (OOH*, HOOH* etc.) intermediate species

dx.doi.org/10.1021/jp5098553 | J. Phys. Chem. C 2015, 119, 757−765

occurring from oxygen reduction in O_2. These additional molecular species apparently can impede adsorption of OH, as the OOH and HOOH compete with OH for Pt sites, so that in the BOL sample the direct contact magnitude arising from OH penetration is reduced in O_2 compared with N_2. Surprisingly for the 10k and 30k $PtNi_3$ samples, the penetration potential does not appear to decrease in O_2 compared to N_2; in contrast to that of PtCo. The reason for this is not clear, but suggests that the adsorbed dioxygen species can either impede or assist OH penetration depending on Pt shell thickness.

Finally Figure 3 shows Ni K-edge data for the SA samples, see Table 1. The precursors for the NA and SA samples were prepared differently from the PtM_3 samples. Note that the NA and SA catalysts have "thicker" Pt skins at BOL as indicated by the higher V_{pen}, which remains relatively high after cycling, while the $PtNi_3$ or similar $PtCo_x$ catalysts have thinner Pt skins at BOL, but then become thicker after 10k and 30k cycles. The annealed SAa catalyst has a very thick Pt skin (V_{pen} > 1.35 V) but it appears to become thinner with cycling so that after 30k cycles V_{pen} has reduced to 1.10 V. Finally note the similar effects of O_2 relative to N_2 for both catalysts in Figure 3; at low potential the $|\Delta\mu|$ is always shifted up due to the larger ligand effect in O_2 because of the additional ORR intermediates, OH, OOH and HOOH, as discussed above; but eventually they merge or cross and the V_{pen} becomes lower like that seen with $PtCo_3$ in Figure 2a, when the additional adsorbates apparently help to penetrate the skin earlier. The differences between that in N_2 and O_2 here for these sc–ns nanoparticles is quite easily understood and expected, in contrast to that for the more complex mc-ps PtM_3 particles above.

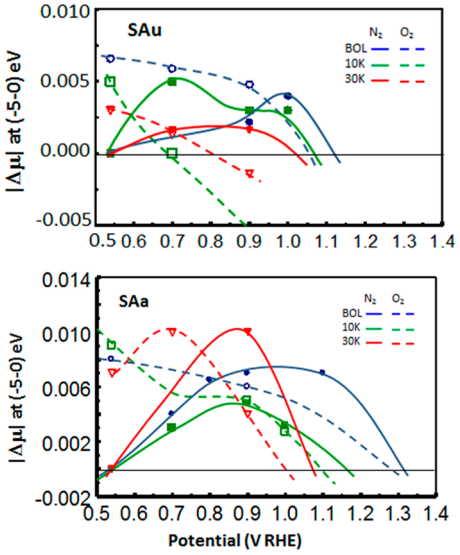

Figure 3. Ni edge $|\Delta\mu|$ for the PtNi catalysts SAu and SAa as indicated. SAu 10k data with only two points may not be significant.

To support the $\Delta\mu$ analysis, HAADF-STEM was used to estimate the Pt-skin thicknesses (Figure 4). Unfortunately, due to the nonuniformity in morphology of many samples, i.e., mc–ps of $PtNi_3$ and $PtCo_3$, not all of the samples were suitable for microscopy analysis. We focused our analyses on the SAu and SAa samples that were shown to have uniform sc–ns structure. Pt-skin thicknesses were defined by the distance between the half intensities of HAADF–STEM (Pt) and of EELS (Ni) from each line scan (Figure 4). As shown in Table 2, the skin thicknesses for SAu and SAa grew from about 1.2 nm at BOL to about 1.6 nm after 30k cycles. The NAu electrocatalysts also exhibited similar skin growth.

Table 2. Measurement of Pt-Shell Thickness Using HAADF–STEM[a]

	BOL	30k cycles
SAu	1.16 ± 0.57	1.59 ± 0.55
SAa	1.27 ± 0.32	1.62 ± 0.49

[a]Thicknesses are shown in nanometers with one-standard deviations.

DISCUSSION

The penetration potential, V_{pen}, as defined above are summarized in Figure 5. All of these data appear to suggest that cycling under the DOE protocol generates a "characteristic" Pt skin robustness. If the Pt skin at BOL is "thin" with V_{pen} < 0.9 V (as in $PtNi_3$ and $PtCo_x$) it grows to a "characteristic" thickness consistent with a V_{pen} of ≈1.1 V; and if it begins very "thick" (i.e., in the case of SAa) it thins to the same "characteristic" thickness. When V_{pen} initiates at 1.1 V, it remains nearly at that value from BOL to EOL. Figure 5 also suggests that there is a fundamental difference in the Pt skin formed by dealloying in H_2SO_4 vs HNO_3 (although impossible to recognize by TEM), as V_{pen} is smaller at BOL in HNO_3

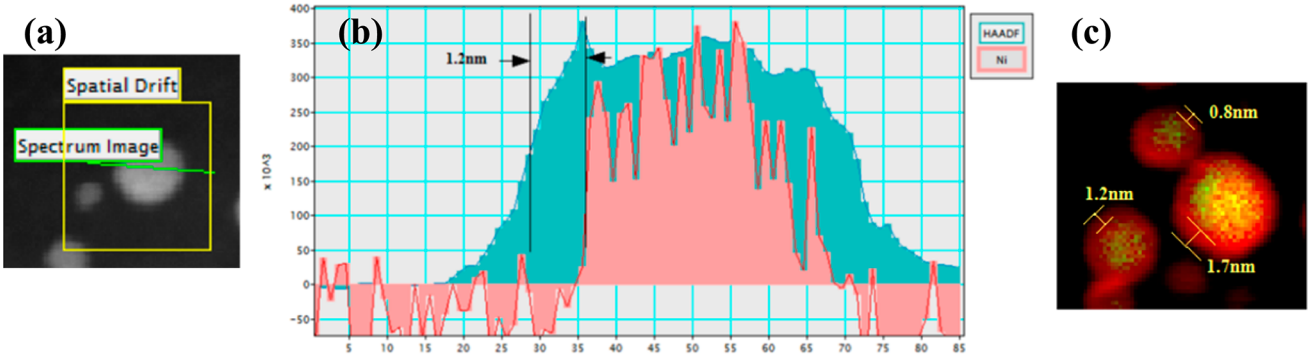

Figure 4. Pt-skin thickness estimate using EELS in the STEM mode on SAu 30K cycled particles. (a) HAADF image of a particle on which the EELS line scan was performed. Green line across the particle marked as "Spectrum Image" is where the data were collected. A drift correction during data collection was made by monitoring the drift of the area in the yellow square marked as "spatial drift". (b) HAADF intensity profile of Pt (red) and Ni (blue) across the line in part a. (c) Examples of overlaid elemental maps of Pt (red) and Ni, green.

dx.doi.org/10.1021/jp5098553 | J. Phys. Chem. C 2015, 119, 757–765

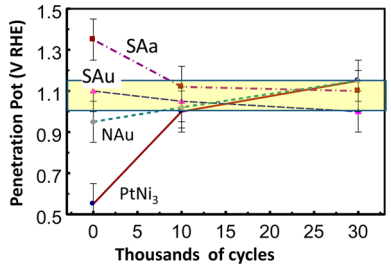

Figure 5. Penetration potential vs number of cycles for four different $PtNi_x$ catalysts as summarized in Table 1. Shaded region indicates "characteristic" V_{pen} or final Pt skin thickness.

regardless of the precursor. H_2SO_4 is a milder oxidant than HNO_3, and thus the slower dealloying process appears to give a more robust well-formed Pt skin. Figure 6 shows how the

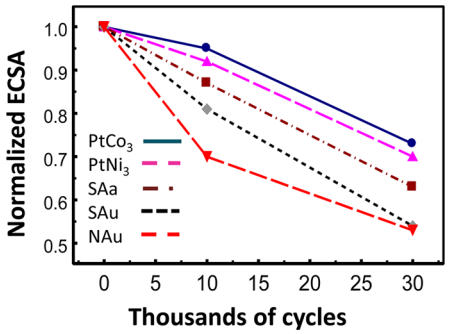

Figure 6. Number of voltage cycles (0.6−1.0 V) vs normalized ECSA (electrochemical surface area, see text).

ECSA (electrochemically active surface area) drops with cycling; this drop arises because the particle size is increasing. Particle size growth via Ostwald ripening is known to result from the oxidation of the Pt and M metals, and subsequent Pt reduction. Clearly, the more durable the particle, the slower the drop in ECSA, indicating the durability increases in the order $PtNi_3$ < NAu < SAu < SAa. One might expect a correlation between durability and V_{pen} because a more durable particle suggests a more robust Pt skin (thickness or porosity) and hence higher V_{pen}. Indeed as indicated by Figure 5, such a correlation is found as V_{pen} increases at the BOL and 10k stages in the order exactly as indicated above for the durability. The $PtCo_3$ is surprisingly stable as suggested by the slow drop in ECSA in Figure 6, second only to SAa, and this indeed suggests that the Pt skin is able to heal very fast in this catalyst, as suggested in the Figure 2A.

Does V_{pen} track the porosity of the Pt skin or its thickness? Both would be expected to significantly affect Pt−O penetration and exchange, and thus influence particle growth, so the correlation between V_{pen} (it robustness) and ECSA noted above does not shed light on this question. However, we can probe the data more closely by looking at the maximum in the $\Delta\mu$ ($\Delta\mu_{max}$) normally occurring around 0.7−1.1 V in N_2. This maximum reflects many factors; namely the ECSA, the Pt/Ni ratio, the specific coverage of O(H) at this potential ($\theta_{O(H)}$) which should be relatively constant, the intrinsic $\Delta\mu$ line shape ($\Delta\mu_{shape}$), and the thickness of the Pt skin (τ):

$$\Delta\mu_{max} \propto \text{ECSA} \times (\text{Pt/Ni}) \times \theta_{O(H)} \times \Delta\mu_{shape}/\tau \quad (2)$$

Here, $\Delta\mu_{max}$ increases with Pt/Ni ratio, because the M k-edge data has been normalized to absorption per M atom, but we are watching coverage on the Pt skin at potentials below V_{pen}, so we want to normalize to Pt content. Further, as long as we are well below V_{pen}, the $\Delta\mu_{shape}$ represents the positive indirect ligand effect, not the negative direct contact shape. Since we want the largest $\Delta\mu_{max}$ reflecting maximum adsorbate coverage, we use the largest of the $\Delta\mu_{max}$ in either O_2 or N_2. To keep $\Delta\mu_{shape}$ nonvariant, we utilize only the data at 10k and 30k for NAu and $PtNi_3$; i.e., when indeed the V_{pen} is around 1.1 V. Finally $\Delta\mu_{max}$ should decrease with Pt skin thickness, because as the Pt skin gets thicker, the average ligand effect per Pt atom in the skin should drop off, as the ligand effect originates from the O(H) or OO(H) adsorption on the outermost Pt surface layer (at least at potentials well below V_{pen}), and must penetrate the Pt skin to alter the μ of the subsurface Co or Ni to be seen experimentally in $\Delta\mu$.

Figure 7 shows a plot of $\Delta\mu_{max}$ vs ECSA*(Pt/Ni), which reveals two different regions with different slopes. The regions

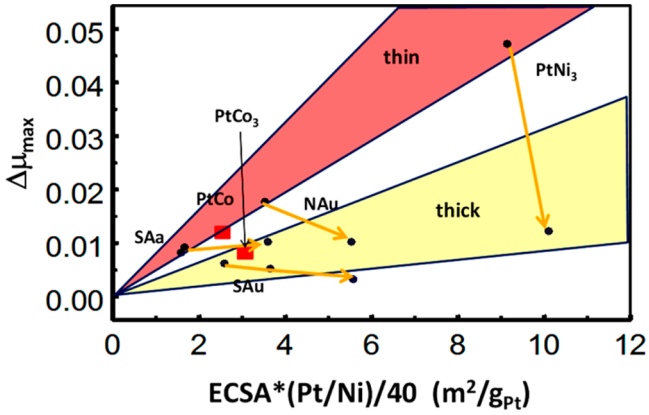

Figure 7. Plot of Ni or Co K edge $\Delta\mu_{max}$ (largest of that in N_2 or O_2) vs ECSA*(Pt/Ni)/40 for the 6 catalysts at different stages of aging. The factor of 40 is introduced only for convenience. Yellow arrows connect the points for the indicated catalysts. Only the 10k and 30k data are indicated for the NAu and $PtNi_3$ catalysts for the reasons indicated in the text when discussing eq 2. The PtCo and $PtCo_3$ (after healing) are indicated by the red squares. Shaded regions indicate region for relatively thin vs thick Pt skins.

indicate the expected dependence on ECSA*(Pt/Ni). As noted above, $\theta_{O(H)}$ and $\Delta\mu_{shape}$ should be relatively unchanging; therefore, the different slopes should reflect different skin thickness, as noted in the figure. Figure 7 shows that upon going from 10k to 30k cycles, the τ increases for both the $PtNi_3$ and NAu as expected, and this is the primary cause for the increase in V_{pen}. The Pt skin begins thicker for the SAu and τ increases still further after reaching 30k cycles. Figure 7 suggests that the annealed SAa particles have a thinner skin, which remains relatively thin even after 30K cycles; however in this region of the plot, the difference between the thin and thick Pt skins are nearly negligible, so this is not clear from Figure 7. STEM-EELS mapping results shown in Table 2 on the SAa and SAu catalysts show that the Pt skin thicknesses are very similar (at BOL, 1.2 ± 0.4 nm and at 30k 1.6 ± 0.4 nm to within statistical error). This would suggest that the higher V_{pen} for the SAa catalyst apparently reflects a particularly nonporous Pt skin, but not necessarily a thicker one. Apparently the postannealing process, carried out as summarized in Table 1

dx.doi.org/10.1021/jp5098553 | J. Phys. Chem. C 2015, 119, 757−765

above, "heals" the Pt skin of the holes, but does not necessarily make it thicker.

Figure 7 also contains the two data points as noted with the red squares for $PtCo_n$. The point for $PtCo_3$ reflects the $\Delta\mu_{max}$ after the apparent "healing" of the porous Pt skin revealed in Figure 2a. This suggest that the Pt skin is still relatively "thin" at this point, but it must get much "thicker" (more robust) with cycling, and quickly, as suggested by the ECSA data in Figure 6, showing surprising durability. It is reasonable to accept that the cycling process, which involves oxidation and reduction of the particle surface thousands of times, results in the observed growth in the particle size (HAADF) and depletion of Ni (EELS data not reported here) from the entire particle and certainly from the particle surface, and thereby growth and "healing" of the Pt skin. However, acquisition of the XANES data involves holding the electrochemical cell at a fixed potential (i.e., 0.54, 0.70, 0.80, 0.90, and 1.00 V) for about 20 min to allow the entire range of XAS data to be collected. This is a much milder process (virtually a few slow cycles vs 10 000s of faster ones), yet the data in Figure 2 suggest that the Pt skin in the $PtCo_3$ and $PtNi_3$ (BOL) catalysts "healed" themselves when the potential was held fixed at around 0.9 V. However, 0.9 V is the very region where O(H) comes on the surface, oxidizes it, and then in a slower process place exchanges with Pt, possibly explaining this time dependent cycling phenomenon. Possibly, in the faster cycling process less place exchange occurs even though more OH comes on the surface. This obviously needs to be examined further.

SUMMARY AND CONCLUSIONS

We have shown in this work that the Co or Ni K-edge $\Delta\mu$-XANES data on dealloyed $PtCo_x$ and $PtNi_x$ catalysts can be used as an *in situ* method to shed light on the nature of the Pt skin, its thickness and porosity, and how it changes under real operating conditions in a fuel cell. Six different catalysts at different stages of life were studied; all meeting the DOE 2017 beginning of life target, but have widely varying durability. The $\Delta\mu$ data are used to determine at what potential (V_{pen}) the Pt skin is penetrated by oxygen. This V_{pen} is found to correlate with durability as indicated by the drop in ECSA data with cycling. Compared to HNO_3, dealloying in H_2SO_4 appears to produce a thicker Pt skin, but a postannealing process applied to a SAu catalysts apparently produces a more robust nonporous skin as opposed to making it thicker. The data indicate that cycling produces a "characteristic" Pt skin "robustness" as indicated by a characteristic penetration potential of 1.1 V. Further, the $PtCo_3$ and $PtNi_3$ catalysts exhibited a skin "healing" process whereby the initial porous skin appears to become less porous after just a hold of the potential at 0.9 V as discussed immediately above. This healing process might explain the relative durability of these catalysts under ORR conditions despite their initial porous skin after dealloying.

AUTHOR INFORMATION

Corresponding Author

*(D.E.R.) E-mail: ramaker@gwu.edu. Telephone: 703-451-4495. Fax: (202) 994-5873.

Author Contributions

‡The manuscript was written through contributions of all authors. All authors have given approval to the final version of the manuscript.

Notes

The authors declare no competing financial interest.

ACKNOWLEDGMENTS

The catalyst precursors were provided by Johnson Matthey (R. O'Malley and A. Martinez). T. E. Moylan (GM) performed the dealloying and MEA tests. Use of the NSLS, Brookhaven National Laboratory, was supported by the US DOE, Office of Science, OBES, under Contract No. DE-AC02-98CH10886. This publication was made possible by a Center for Synchrotron Biosciences grant, P30-EB-00998, from the National Institute of Biomedical Imaging and Bioengineering. Primary funding for this research was provided by the Energy Efficiency and Renewable Energy Office of the US DOE under Contract DE-EE0000458

REFERENCES

(1) Dresselhaus, M. S.; Thomas, I. L. Alternative Energy Technologies. *Nature* **2001**, *414*, 332−337.
(2) Steele, B. C.H.; Heinzel, A. Materials for Fuel-cell Technologies. *Nature* **2001**, *414*, 345−352.
(3) Lefèvre, M.; Proietti, E.; Jaouen, F.; Dodelet, J.-P. Iron-Based Catalysts with Improved Oxygen Reduction Activity in Polymer Electrolyte Fuel Cells. *Science* **2009**, *324*, 71−74.
(4) Gasteiger, H. A.; Markovi, N. M. Just a Dream or Future Reality? *Science* **2009**, *324*, 48−49.
(5) Adzic, R. R. Recent Advances in the Kinetics of Oxygen Reduction, in *Electrocatalysis*; Lipkowski, J., Ross, P. N., Eds.; Wiley VCH: New York, 1998; p 197−241.
(6) Gasteiger, H. A.; Kocha, S. S.; Sompalli, B.; Wagner, F. T. Activity Benchmarks and Requirements for Pt, Pt-alloy, and non-Pt Oxygen Reduction Catalysts for PEMFCs. *Appl. Catal., B* **2005**, *56*, 9−35.
(7) Vante, N. A.; Tributsch, H. Energy Conversion Catalysis using Semiconducting Transition Metal Cluster Compounds. *Nature* **1986**, *323*, 431−432.
(8) Teliska, M.; Murthi, V. S.; Mukerjee, S.; Ramaker, D. E. Correlation of Water Activation, Surface Properties, and Oxygen Reduction Reactivity of Supported Pt−M/C Bimetallic Electrocatalysts Using XAS. *J. Electrochem. Soc.* **2005**, *152A*, 2159−2169.
(9) Vielstich, W.; Paganin, V. A.; Alves, O. B.; Ciapina, E. G. On the Pathways of Methanol and Ethanol Oxidation In *Handbook of Fuel Cells: Fundamentals, Technology, and Applications*; Wiley: Hoboken, NJ, 2003.
(10) US Council for Automotive Research, LLC, US Drive Fuel Cell Tech Team, accessed Feb 13, 2014, http://www.uscar.org/guest/teams/17/U-S-DRIVE-Fuel-Cell-Tech-Team.
(11) Strasser, P.; Koh, S.; Anniyev, T.; Greeley, J.; More, K.; Yu, C.; Liu, Z.; Kaya, S.; Nordlund, D.; Ogasawara, H.; et al. Lattice-strain Control of the Activity in Dealloyed Core−shell Fuel Cell Catalysts. *Nat. Chem.* **2010**, *2*, 454−460.
(12) Stamenkovic, V. R.; Fowler, B.; Mun, B. S.; Wang, G. F.; Ross, P. N.; Lucas, C. A.; Markovic, N. M. Improved Oxygen Reduction Activity on $Pt_3Ni(111)$ via Increased Surface Site Availability. *Science* **2007**, *315*, 493−497.
(13) Stamenkovic, V. R.; Mun, B. S.; Arenz, M.; Mayrhofer, K. J. J.; Lucas, C. A.; Wang, G. F.; Ross, P. N.; Markovic, N. M. Trends in Electrocatalysis on Extended and Nanoscale Pt-Bimetallic Alloy Surfaces. *Nat. Mater.* **2007**, *6*, 241−247.
(14) Stamenkovic, V. R.; Mun, B. S.; Mayrhofer, K. J. J.; Ross, P. N.; Markovic, N. M. Effect of Surface Composition on Electronic Structure, Stability, and Electrocatalytic Properties of Pt-Transition Metal Alloys: Pt-Skin versus Pt-Skeleton Surfaces. *J. Am. Chem. Soc.* **2006**, *128*, 8813−8819.
(15) Stephens, I. E. L.; Bondarenko, A. S.; Perez-Alonso, F. J.; Calle-Vallejo, F.; Bech, L.; Johansson, T. P.; Jepsen, A. K.; Frydendal, R.; Knudsen, B. P.; Rossmeisl, J. I.; et al. Tuning the Activity of Pt(111)

for Oxygen Electroreduction by Subsurface Alloying. *J. Am. Chem. Soc.* **2011**, *133*, 5485−5491.
(16) Wang, C.; van der Vliet, D.; Chang, K. C.; You, H. D.; Strmcnik, D.; Schlueter, J. A.; Markovic, N. M.; Stamenkovic, V. R. Monodisperse Pt_3Co Nanoparticles as a Catalyst for the Oxygen Reduction Reaction: Size-Dependent Activity. *J. Phys. Chem. C* **2009**, *113*, 19365−19368.
(17) Wang, C.; Wang, G. F.; van der Vliet, D.; Chang, K. C.; Markovic, N. M.; Stamenkovic, V. R. Monodisperse Pt_3Co Nanoparticles as Electrocatalyst: The Effects of Particle Size and Pretreatment on Electrocatalytic Reduction of Oxygen. *Phys. Chem. Chem. Phys.* **2010**, *12*, 6933−6939.
(18) Chen, S.; Sheng, W. C.; Yabuuchi, N.; Ferreira, P. J.; Allard, L. F.; Shao-Horn, Y. Origin of Oxygen Reduction Reaction Activity on "Pt_3Co" Nanoparticles: Atomically Resolved Chemical Compositions and Structures. *J. Phys. Chem. C* **2009**, *113*, 1109−1125.
(19) Skulason, E.; Tripkovic, V.; Bjorketun, M. E.; Gudmundsdottir, S.; Karlberg, G.; Rossmeisl, J.; Bligaard, T.; Jonsson, H.; Norskov, J. K. Modeling the Electrochemical Hydrogen Oxidation and Evolution Reactions on the Basis of Density Functional Theory Calculations. *J. Phys. Chem. C* **2010**, *114*, 18182−18197.
(20) Hasche, F.; Oezaslan, M.; Strasser, P. Activity, Structure and Degradation of Dealloyed $PtNi_3$ Nanoparticle Electrocatalyst for the Oxygen Reduction Reaction in PEMFC. *J. Electrochem. Soc.* **2012**, *159*, B24−B33.
(21) Jia, Q.; Segre, C. U.; Ramaker, D. E.; Caldwell, K.; Trahan, M.; Mukerjee, S. Structure−Property−Activity Correlations of Pt-Bimetallic Nanoparticles: A Theoretical Study. *Electrochim. Acta* **2013**, *88*, 604−613.
(22) Mukerjee, S.; Srinivasan, S. J. Enhanced Electrocatalysis of Oxygen Reduction on Platinum Alloys in Proton Exchange Membrane Fuel Cells. *Electroanal. Chem.* **1993**, *357*, 201−224.
(23) Mukerjee, S.; Srinivasan, S.; Soriaga, M. P.; Mcbreen, J. Effect of Preparation Conditions of Pt Alloys on Their Electronic, Structural, and Electrocatalytic Activities for Oxygen Reduction - XRD, XAS, and Electrochemical Studies. *J. Phys. Chem.* **1995**, *99*, 4577−4589.
(24) Min, M. K.; Cho, J. H.; Cho, K. W.; Kim, H. Particle Size and Alloying Effects of Pt-based Alloy Catalysts for Fuel Cell Applications. *Electrochim. Acta* **2000**, *47*, 4211−4217.
(25) Paulus, U. A.; Wokaun, A.; Scherer, G. G.; Schmidt, T. J.; Stamenkovic, V.; Markovic, N. M.; Ross, P. N. Oxygen Reduction on High Surface Area Pt-based Alloy Catalysts in Comparison to Well Defined Smooth Bulk Alloy Electrodes. *Electrochim. Acta* **2002**, *47*, 3787−3798.
(26) Paulus, U. A.; Wokaun, A.; Scherer, G. G.; Schmidt, T. J.; Stamenkovic, V.; Radmilovic, V.; Markovic, N. M.; Ross, P. N. Oxygen Reduction on Carbon-Supported Pt−Ni and Pt−Co Alloy Catalysts. *J. Phys. Chem. B* **2002**, *106*, 4181−4191.
(27) Soderberg, J. N.; Sirk, A. H. C.; Campbell, S. A.; Birss, V. I. Oxygen Reduction by Sol-Derived Pt/Co -Based Alloys for PEM Fuel Cells. *J. Electrochem. Soc.* **2005**, *152*, A2017−A2022.
(28) Qian, Y. D.; Wen, W.; Adcock, P. A.; Jiang, Z.; Hakim, N.; Saha, M. S.; Mukerjee, S. J. PtM/C Catalyst Prepared Using Reverse Micelle Method for Oxygen Reduction Reaction in PEM Fuel Cells. *Phys. Chem. C* **2008**, *112*, 1146−1157.
(29) Hwang, B. J.; Kumar, S. M. S.; Chen, C.-H.; Cheng, M.-Y.; Liu, D.-G.; Lee, J.-F. An Investigation of Structure−Catalytic Activity Relationship for Pt−Co/C Bimetallic Nanoparticles toward the Oxygen Reduction Reaction. *J. Phys. Chem. C* **2007**, *111*, 15267−15276.
(30) Kongkanand, A.; , 2013 Annual Merit Review, US Department of Energy Hydrogen and Fuel Cells Program, accessed Feb 13, 2014, http://www.hydrogen.energy.gov/pdfs/review13/fc087_kongkanand_2013_o.pdf.
(31) Debe, M. K. Electrocatalyst Approaches and Challenges for Automotive Fuel Cells. *Nature* **2012**, *486*, 43−51.
(32) Greely, J.; Stephens, I. E. L.; Bondarenko, A. S.; Johensson, T. P.; Hansen, H. A.; Jaramillo, T. F.; Rossmeisl, J.; Chorkendorff, I.; Norskov, J. K. Alloys of Platinum and Early Transition Metals as Oxygen Reduction Electrocatalysts. *Nat. Chem.* **2009**, *1*, 552−556.
(33) Scott, F. J.; Mukerjee, S.; Ramaker, D. E. CO Coverage/Oxidation Correlated with PtRu Electrocatalyst Particle Morphology in 0.3 M Methanol by In Situ XAS. *J. Electrochem. Soc.* **2007**, *154*, A396−A406.
(34) Roth, C.; Benker, N.; Buhrmester, T.; Mazurek, M.; Loster, M.; Fuess, H.; Koningsberger, D. C.; Ramaker, D. E. Determination of O[H] and CO Coverage and Adsorption Sites on PtRu Electrodes in an Operating PEM Fuel Cell. *J. Am. Chem. Soc.* **2005**, *127*, 14607−14615.
(35) Wiltshire, R. J. K.; King, C. R.; Rose, A.; Wells, P. P.; Hogarth, M. P.; Thompsett, D.; Russell, A. E.; PEM, A. fuel cell for in situ XAS studies. *Electrochim. Acta* **2005**, *50*, 5208−5217.
(36) Roth, C.; Martz, N.; Buhrmester, T.; Scherer, J.; Fuess, H. In-situ XAFS Fuel Cell Measurements of a Carbon-Supported Pt−Ru Anode Electrocatalyst in Hydrogen and Direct Methanol Operation. *Phys. Chem. Chem. Phys.* **2002**, *4*, 3555−3557.
(37) Scott, F. J.; Roth, C.; Ramaker, D. E. Kinetics of CO Poisoning in Simulated Reformate and Effect of Ru Island Morphology on PtRu Fuel Cell Catalysts As Determined by Operando X-ray Absorption Near Edge Spectroscopy. *J. Phys. Chem. C* **2007**, *111*, 11403−11413.
(38) Teliska, M.; O'Grady, W. E.; Ramaker, D. E. Determination of H Adsorption Sites on Pt/C Electrodes in $HClO_4$ from Pt L_{23} X-ray Absorption Spectroscopy. *J. Phys. Chem. B* **2004**, *108*, 2333.
(39) Teliska, M.; O'Grady, W. E.; Ramaker, D. E. Determination of O and OH Adsorption Sites and Coverage in Situ on Pt Electrodes from Pt L_{23} X-ray Absorption Spectroscopy. *J. Phys. Chem. B* **2005**, *109*, 8076.
(40) Hammer, B.; Norskov, J. K. Theoretical Surface Science and Catalysis—Calculations and Concepts. *Adv. Catal.* **2000**, *45*, 71−129.
(41) Sabatier, P. Hydrogénations et déshydrogénations par catalyse. *Ber. Dtsch. Chem. Ges.* **1911**, *44*, 1984−2001.
(42) Casalongue, H. S.; Kaya, S.; Viswanathan, V.; Miller, D. J.; Friebel, D.; Hansen, H. A.; Norskov, J. K.; Nilsson, A.; Ogasawara, H. Direct Observation of the Oxygenated Species During Oxygen Reduction on a Platinum Fuel Cell Cathode. *Nat. Commun.* **2013**, *4*, 2817.
(43) Jia, Q.; Caldwell, K.; Zeigelbauer, J.; Kongkanand, A.; Wagner, F. T.; Mukerjee, S.; Ramaker, D. E. The Role of OOH Binding Site and Pt Surface Structure on ORR Activities. *J. Electrochem. Soc.* **2014**, *162*, F1323−F1329.
(44) Jia, Q.; Caldwell, K.; Ramaker, D. E.; Ziegelbauer, J. M.; Liu, Z.; Yu, Z.; Trahan, M.; Mukerjee, S. In Situ Spectroscopic Evidence for Ordered Core−Ultrathin Shell Pt_1Co_1 Nanoparticles with Enhanced Activity and Stability as Oxygen Reduction Electrocatalysts. *J. Phys. Chem. C* **2014**, *118*, 20496−20503.
(45) Arruda, T.; Shyam, B.; Lawton, J.; Ramaswamy, N.; Budil, D.; Ramaker, D. E.; Mukerjee, S. Fundamental Aspects of Spontaneous Cathodic Deposition of Ru onto Pt/C Electrocatalysts and Membranes under Direct Methanol Fuel Cell Operating Conditions: An in Situ X-ray Absorption Spectroscopy and Electron Spin Resonance Study. *J. Phys. Chem. C* **2010**, *114*, 1028−1040.
(46) Ravel, B.; Newville, M. J. ATHENA, ARTEMIS, HEPHAESTUS: Data analysis for X-ray Absorption Spectroscopy using IFEFFIT. *J. Synch. Rad.* **2005**, *12*, 537−541.
(47) Newville, M. J. IFEFFIT: Interactive XAFS analysis and FEFF Fitting. *J. Synch. Rad.* **2001**, *8*, 322−324.
(48) Ankudinov, A. L.; Ravel, B.; Rehr, J. J.; Conradson, S. D. Real-space Multiple-Scattering Calculation and Interpretation of X-ray Absorption Near-edge Structure. *Phys. Rev. B* **1998**, *58*, 7565−7576.
(49) Janin, E.; von Schenck, H.; Göthelid, M.; Karlsson, U. O.; Svensson, M. Bridge-Bonded Atomic Oxygen on Pt(110). *Phys. Rev. B* **2000**, *61*, 13144−13149.
(50) Liu, Z.; Xin, H.; Yu, Z.; Zhu, Y.; Zhang, J.; Mundy, J. A.; Muller, D. A.; Wagner, F. T. Atomic-Scale Compositional Mapping and 3-Dimensional Electron Microscopy of Dealloyed $PtCo_3$ Catalyst Nanoparticles with Spongy Multi-Core/Shell Structures. *J. Electrochem. Soc.* **2012**, *159*, F554−F559.

(51) Yu, Z.; Zhang, J.; Liu, J.; Ziegelbauer, J. M.; Xin, H.; Dutta, I.; Muller, D. A.; Wagner, F. W. Comparison between Dealloyed $PtCo_3$ and $PtCu_3$ Cathode Catalysts for Proton Exchange Membrane Fuel Cells. *J. Phys. Chem. C* **2012**, *116*, 19877−19885.
(52) Han, B.; Carlton, C. E.; Kongkanand, A.; Kukreja, R. S.; Theobald, B. R.; Gan, L.; O'Malley, R.; Strasser, P.; Wagner, F. T.; Shao-Horn, Y. Record Activity and Stability of Dealloyed Bimetallic Catalysts for Proton Exchange Membrane Fuel Cells. *Energy Environ. Sci.* **2015**, DOI: 10.1039/C4EE02144D.